

A visibility-based angular bispectrum estimator for radio-interferometric data

SUKHDEEP SINGH GILL ¹, SOMNATH BHARADWAJ ¹, SK. SAIYAD ALI ² AND KHANDAKAR MD ASIF ELAHI ³

¹*Department of Physics, Indian Institute of Technology Kharagpur, Kharagpur 721 302, India*

²*Department of Physics, Jadavpur University, Kolkata 700032, India*

³*Centre for Strings, Gravitation and Cosmology, Department of Physics, Indian Institute of Technology Madras, Chennai 600036, India*

ABSTRACT

Considering radio-interferometric observations, we present a fast and efficient estimator to compute the binned angular bispectrum (ABS) from gridded visibility data. The estimator makes use of Fast Fourier Transform (FFT) techniques to compute the bispectrum covering all possible triangle shapes and sizes. Here, we present the formalism of the estimator and validate it using simulated visibility data for the Murchison Widefield Array (MWA) observations at $\nu = 154.25$ MHz. We find that our estimator is able to faithfully recover the ABS of the simulated sky signal with $\approx 10 - 15\%$ accuracy for a wide variety of triangle shapes and sizes across the range of angular multipoles $46 \leq \ell \leq 1320$. In future work, we plan to apply this to actual data and also generalize it to estimate the three-dimensional redshifted 21-cm bispectrum.

Keywords: methods: statistical, data analysis – technique: interferometric –(cosmology:) diffuse radiation

1. INTRODUCTION

There is considerable motivation to quantify the statistics of the sky signal at radio-wavelengths. Radio interferometric observations of the redshifted 21-cm signal from neutral hydrogen (H I) hold the potential to probe a wide range of cosmological and astrophysical phenomena in a large redshift range (Bharadwaj & Ali 2005). In particular, several radio-interferometers, such as MWA¹ (Tingay et al. 2013), LOFAR² (van Haarlem, M. P. et al. 2013), and HERA³ (De-Boer et al. 2017) are currently involved in efforts to detect the Epoch of Reionization (EoR) redshifted 21-cm signal in the frequency range 100 – 200 MHz. Much of the observational effort so far has focused on the power spectrum (PS). Despite continued efforts, the EoR 21-cm PS remains to be detected, and the lowest upper limit at present is $\Delta^2(k) < (30.76)^2 \text{ mK}^2$ at $k = 0.192 h \text{ Mpc}^{-1}$ for $z = 7.9$ from the HERA (The HERA Collaboration, 2022).

The PS, which quantifies the square of the amplitude of different Fourier modes, is adequate if the signal is a Gaussian random field that is completely quantified by its second-order

statistics. However, the EoR 21-cm signal is predicted to be highly non-Gaussian (Bharadwaj & Pandey 2005). The PS completely misses the correlations between the phases of different modes. It is also oblivious to the geometry and topology (e.g., Bag et al. 2018, 2019) of structures in the non-Gaussian field. The bispectrum (BS) is the lowest-order statistic that is sensitive to the non-Gaussianity. A measurement of the EoR 21-cm BS has the potential to capture considerable information that is missed by the PS (Bharadwaj & Pandey 2005). Considerable effort has been made to predict the BS using simulations (Majumdar et al. 2018; Watkinson et al. 2019; Majumdar et al. 2020; Kamran et al. 2021; Gill et al. 2024). Several studies show that the BS undergoes a sign change as the topology of the H I field evolves. The first sign flip occurs at the early stage of the EoR, which serves as a valuable indicator of the emergence of distinct ionized bubbles in the neutral background (Majumdar et al. 2018). The second sign change, which occurs at the end stage of the EoR, indicates a further topological shift, where isolated H I islands emerge within a largely ionized background (Raste et al. 2023; Gill et al. 2024). Furthermore, the quadrupole moment of the BS is sensitive to the model of the EoR, and it holds the potential to distinguish between inside-out and outside-in scenarios of the EoR (Gill et al. 2024). The inclusion of the 21-cm BS along with the PS also improves constraints on the EoR model parameters (Shimabukuro et al. 2017; Watkinson et al. 2022). There is also considerable motivation to measure the 21-cm BS from other cosmological epochs like the Dark Ages (Pillepich et al.

Corresponding author: Sukhdeep Singh Gill
sukhdeepsingh5ab@gmail.com

¹ <https://www.mwatelescope.org/>

² <https://www.astron.nl/telescopes/lofar/>

³ <https://reionization.org/>

2007; Cooray et al. 2008) and the post-reionization era (Ali et al. 2006; Sarkar et al. 2019).

Trott et al. (2019) have estimated the 21-cm bispectrum from data taken as part of the EoR project of the MWA. In their study, they have considered equilateral and isosceles triangles, and found that the thermal noise level is achieved in 10 h of observations for the case of large-scale isosceles triangles. They propose that the BS may be detectable with lesser observational time than the PS for radio-interferometers with dense uv coverage. To the best of our knowledge, this is the only observational attempt to measure the 21-cm BS.

In this paper we present the first step towards systematically developing a fast BS estimator considering triangles of all possible shapes and sizes. The analysis here is restricted to a single frequency, and we entirely focus on estimating the two-dimensional (2D) angular bispectrum (ABS). We plan to consider multi-frequency observations and the three-dimensional (3D) BS in future work. The idea is to proceed in two steps, similar to the approach adopted earlier for the PS where Choudhuri et al. (2014) considered the angular power spectrum (APS) at a single frequency, and Bharadwaj et al. (2018) extended this to the 3D PS considering multi-frequency observations.

It is worth noting that the ABS is of considerable interest in its own right. For example, there have been several efforts to probe the APS of the ~ 150 MHz sky signal using radio-interferometers, both to characterize the foregrounds for the 21-cm PS measurements and to study the diffuse Galactic synchrotron emission e.g., (Ali et al. 2008; Bernardi et al. 2009; Ghosh et al. 2012). There is also considerable interest in measuring the APS of 21-cm emission from H I in the interstellar medium of galaxies (Begum et al. 2006; Dutta et al. 2009), and also the continuum emission from ionized gas in supernova remnants (Roy et al. 2009; Saha et al. 2019; Saha et al. 2021). In all of these contexts, it would be very interesting to enhance our knowledge by including studies of the ABS.

In this work, we present a visibility-based estimator for the ABS $B(\ell_1, \ell_2, \ell_3)$. The estimator uses gridded visibilities to compute the binned ABS using a fast FFT-based technique (Sefusatti 2005; Jeong 2010; Scoccimarro 2015) considering triangles of all possible shapes and sizes. In this work, we present the formalism of the estimator and validate it using simulated MWA observations at $\nu = 154.25$ MHz.

The paper is organized as follows. In Section 2, we present the mathematical formalism of the estimator, and in Section 3 we discuss our method for validating the estimator. We present the results in Section 4, whereas we present a summary and conclusions in Section 5.

2. BISPECTRUM ESTIMATOR

We consider the brightness temperature fluctuations $\delta T_b(\boldsymbol{\theta})$ from a region of the sky that subtends a solid angle $\Omega \ll 1$ that is sufficiently small so that it may be approximated as a two-dimensional (2D) plane. We also express this in terms of Fourier components $\Delta\tilde{T}_b(\boldsymbol{\ell})$,

$$\delta T_b(\boldsymbol{\theta}) = \Omega^{-1} \sum_{\boldsymbol{\ell}} \exp[-i\boldsymbol{\ell} \cdot \boldsymbol{\theta}] \Delta\tilde{T}_b(\boldsymbol{\ell}), \quad (1)$$

where $\boldsymbol{\ell}$, which is the Fourier conjugate of $\boldsymbol{\theta}$, may also be interpreted in terms of the angular multipole $\ell = |\boldsymbol{\ell}|$. Note that the entire analysis here is restricted to a single frequency ν (and wavelength λ) which we do not show explicitly as an argument. Considering $\delta T_b(\boldsymbol{\theta})$ to be a statistically homogeneous and isotropic random field, we have the angular power spectrum (APS)

$$C_\ell = \Omega^{-1} \langle \Delta\tilde{T}_b(\boldsymbol{\ell}) \Delta\tilde{T}_b^*(\boldsymbol{\ell}) \rangle \quad (2)$$

and the angular bispectrum (ABS)

$$B(\ell_1, \ell_2, \ell_3) = \Omega^{-1} \langle \Delta\tilde{T}_b(\boldsymbol{\ell}_1) \Delta\tilde{T}_b(\boldsymbol{\ell}_2) \Delta\tilde{T}_b(\boldsymbol{\ell}_3) \rangle, \quad (3)$$

where $\boldsymbol{\ell}_1 + \boldsymbol{\ell}_2 + \boldsymbol{\ell}_3 = 0$ *i.e.* they form a closed triangle, and the angular brackets $\langle \dots \rangle$ denote an ensemble average over independent realizations of the random field. Note that C_ℓ only depends on magnitude $\ell = |\boldsymbol{\ell}|$, and $B(\ell_1, \ell_2, \ell_3)$ only depends on the shape and size of the triangle which is entirely specified by (ℓ_1, ℓ_2, ℓ_3) the lengths of the three sides respectively. Considering $\ell_1 \geq \ell_2 \geq \ell_3$, here we use ℓ_1 to quantify the size, and the dimensionless parameters $\mu = -(\boldsymbol{\ell}_1 \cdot \boldsymbol{\ell}_2)/(\ell_1 \ell_2)$ and $t = \ell_2/\ell_1$ to quantify the shape of the triangle. The allowed parameter values are constrained to the range $0.5 \leq \mu, t \leq 1$ with $2\mu t \geq 1$, and the reader is referred to Bharadwaj et al. (2020) for a detailed discussion of this parametrization of the bispectrum $B(\ell_1, \mu, t)$.

The $\mathcal{V}(\mathbf{U})$ visibilities measured in radio interferometric observations are a sum of the sky signal and the system noise. In the present work, we have focused on the sky signal and ignored the system noise. As mentioned earlier, we have adopted the flat-sky approximation which treats the region of the sky under observation as a flat 2D plane. We further assume a coplanar radio interferometric array pointing vertically upwards. We then have

$$\mathcal{V}(\mathbf{U}) = Q \int d^2\theta A(\boldsymbol{\theta}) \delta T(\boldsymbol{\theta}) \exp[i2\pi\mathbf{U} \cdot \boldsymbol{\theta}] \quad (4)$$

where the 2D vector \mathbf{U} , with components (u, v) , is a baseline, Q is the Rayleigh-Jeans factor $Q = 2k_B/\lambda^2$ conversion factor from brightness temperature to specific intensity, and $A(\boldsymbol{\theta})$ is the antenna primary beam pattern, which typically is not known a priori. Although this can be estimated from observations (Line et al. 2018; Nunhokee et al. 2020; Virone et al. 2022), it is often useful to consider simple models for $A(\boldsymbol{\theta})$

(e.g., Bharadwaj & Sethi 2001; Choudhuri et al. 2014). For the work presented here, we consider the Murchison Wide-field Array (MWA, Wayth et al. 2018) at $\nu = 154.25$ MHz. It is possible to model each MWA tile as a square aperture of $d = 4$ m, whereby (Line et al. 2018; Chatterjee et al. 2023)

$$A(\boldsymbol{\theta}) = \text{sinc}^2\left(\frac{\pi d \theta_x}{\lambda}\right) \text{sinc}^2\left(\frac{\pi d \theta_y}{\lambda}\right), \quad (5)$$

for which the FWHM of the primary beam is $\theta_F = 24.68$ deg.

Following Choudhuri et al. (2014), it is useful to approximate $A(\boldsymbol{\theta})$ as Gaussian to analytically compute the relations between visibility correlations and the statistics of the sky signal, and we use

$$A_G(\boldsymbol{\theta}) = \exp[-\theta^2/\theta_0^2] \quad (6)$$

where $\theta_0 = 0.6\theta_F$. This approximation holds well at small angles, within $\theta \leq \theta_F$. At large baselines ($U \gg 1/\theta_0$), we then have (see appendix A for a derivation)

$$\langle \mathcal{V}(\mathbf{U}) \mathcal{V}^*(\mathbf{U} + \Delta\mathbf{U}) \rangle = \frac{\pi \theta_0^2 Q^2}{2} \exp[-\pi^2 \theta_0^2 \Delta U^2 / 2] C_\ell \quad (7)$$

which relates the two visibility correlation to the APS C_ℓ with $\ell = 2\pi U$. We do not expect Eq. (7) to hold at small baselines $U \leq 1/\theta_0$, where it is necessary to consider the convolution of C_ℓ with the Fourier transform of $A(\boldsymbol{\theta})$. The reader is referred to Choudhuri et al. (2014) for a detailed discussion of the derivation and application of this relation.

The three visibility correlation is similarly related to the ABS, and at large baselines we have (see appendix A for a derivation)

$$\begin{aligned} \langle \mathcal{V}(\mathbf{U}_1) \mathcal{V}(\mathbf{U}_2) \mathcal{V}(\mathbf{U}_3 + \Delta\mathbf{U}) \rangle \\ = \frac{\pi \theta_0^2 Q^3}{3} \exp[-\pi^2 \theta_0^2 \Delta U^2 / 3] B(\ell_1, \ell_2, \ell_3). \end{aligned} \quad (8)$$

We do not expect this equation to hold at small baselines ($U \leq 1/\theta_0$), where it is necessary to consider the convolution of $B(\ell_1, \ell_2, \ell_3)$ with the Fourier transform of $A(\boldsymbol{\theta})$. Here, $\mathbf{U}_1 + \mathbf{U}_2 + \mathbf{U}_3 = 0$ forms a closed triangle, and $\Delta\mathbf{U}$ is the deviation from a closed triangle configuration. We see that the correlation is strongest when $\Delta\mathbf{U} = 0$, and it falls off rapidly as $\Delta\mathbf{U}$ increases. There is negligible correlation for $\Delta U \geq (\pi\theta_0)^{-1}$. Here, we have used Eq. (8) to define a visibility-based binned angular bispectrum estimator.

To proceed further, we introduce a square grid of spacing ΔU_g in the (u, v) plane, and assign each visibility $\mathcal{V}(\mathbf{U}_i)$ to the grid point \mathbf{U}_g nearest to \mathbf{U}_i using

$$\mathcal{V}_g = \sum_i^{N_g} \tilde{w}(\mathbf{U}_g - \mathbf{U}_i) \mathcal{V}(\mathbf{U}_i), \quad (9)$$

and use N_g to denote the number of visibilities contributing at any grid point g .

For the present work, we have considered the baseline distribution corresponding to a particular pointing of the drift scan observations presented in Patwa et al. (2021) and also analyzed in Chatterjee et al. (2023) and Chatterjee et al. (2024). Fig. 1 shows N_g corresponding to the gridded visibilities for this data. Here, we use the gridded visibilities \mathcal{V}_g to estimate the bispectrum. The computation scales as $\sim N_t^4$, where N_t is the total number of grids, if we evaluate this directly by correlating all possible triplets of grid points that form a closed triangle. The computation can be reduced to $\sim N_t^2 \log N_t^2$ by utilizing FFT techniques introduced by (Sefusatti et al. 2006; Scoccimarro 2015). Here we follow Shaw et al. (2021) to present an FFT based fast estimator for the binned angular bispectrum $B(\ell_1, \mu, t)$.

We divide the \mathbf{U} plane into annular rings. Three such rings, labeled (a_1, a_2, a_3) with mean radii (U_1, U_2, U_3) respectively, are illustrated in Fig. 1. Considering any ring a_m , we define

$$D(\ell_m, \boldsymbol{\theta}) = \sum_{g \in a_m} W_g \mathcal{V}_g \exp(-i\boldsymbol{\ell}_g \cdot \boldsymbol{\theta}), \quad (10)$$

which is the inverse Fourier Transform of \mathcal{V}_g restricted to the annular ring a_m , with $\boldsymbol{\ell}_g = 2\pi\mathbf{U}_g$ and $\ell_m = 2\pi U_m$. Note that we have introduced weights W_g for the gridded visibilities \mathcal{V}_g , these can be adjusted to optimize the signal to noise ratio of the estimated bispectrum. Here, we have not included the system noise contribution, and we use $W_g = N_g^{-1}$ and 0 for the filled and empty grids, respectively. We similarly define

$$I(\ell_m, \boldsymbol{\theta}) = \sum_{g \in a_m} W_g \exp(-i\boldsymbol{\ell}_g \cdot \boldsymbol{\theta}). \quad (11)$$

which is the inverse Fourier Transform of W_g restricted to the annular ring a_m . Following Shaw et al. (2021), we use a combination of three rings (a_1, a_2, a_3) with $\ell_1 \geq \ell_2 \geq \ell_3$, to define the binned angular bispectrum estimator

$$\hat{B}(\ell_1, \ell_2, \ell_3) = \frac{1}{A} \frac{\sum_{\boldsymbol{\theta}} D(\ell_1, \boldsymbol{\theta}) D(\ell_2, \boldsymbol{\theta}) D(\ell_3, \boldsymbol{\theta})}{\sum_{\boldsymbol{\theta}} I(\ell_1, \boldsymbol{\theta}) I(\ell_2, \boldsymbol{\theta}) I(\ell_3, \boldsymbol{\theta})}. \quad (12)$$

where $A = \pi\theta_0^2/3$ is a normalization constant (Eq. 8).

The estimator considers all closed triangles $\mathbf{U}_{g1} + \mathbf{U}_{g2} + \mathbf{U}_{g3} = 0$ such that $(\mathbf{U}_{g1}, \mathbf{U}_{g2}, \mathbf{U}_{g3})$ are within the annular rings (a_1, a_2, a_3) respectively, and it provides the weighted average over all such triangles. One such triangle is illustrated in Fig. 1. We refer to this weighted average (Eq. 12) as the binned angular bispectrum estimator $\hat{B}(\ell_1, \mu, t)$ where ℓ_1 quantifies the average size of the triangles in the bin, and the parameters $\mu = (\ell_1^2 + \ell_2^2 - \ell_3^2)/(2\ell_1\ell_2)$ and $t = \ell_2/\ell_1$ together quantify the average shape of the triangles in the bin.

We note that the system noise contribution to the different visibilities are uncorrelated, and we have $B(\ell_1, \mu, t) = \langle \hat{B}(\ell_1, \mu, t) \rangle \equiv \langle \hat{B}(\ell_1, \ell_2, \ell_3) \rangle$ even if the system noise contribution is taken into account. However, the system noise will

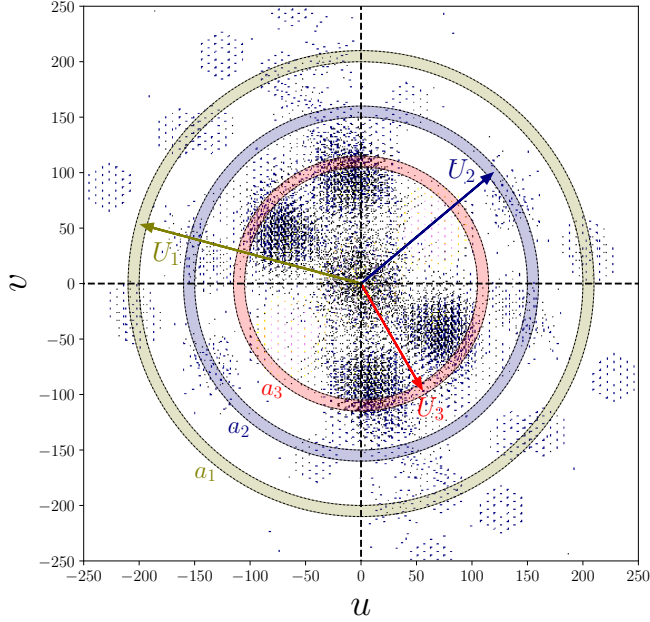


Figure 1. The binning scheme of the estimator. The scattered dots show the discrete sampling of (u, v) space (gridded baseline distribution \mathbf{U}_g) corresponding to a particular pointing of the drift scan observation of the MWA telescope at $\nu = 154.25$ MHz. The \mathbf{U} space is divided into several annular rings. Three such rings (labeled as a_1, a_2, a_3) with average radius (U_1, U_2, U_3) are shown here schematically. The combination of these three rings corresponds to a set of triangles having unique shapes and sizes, and defines a single bin of triangles. One such triangle formed by three discrete modes $\mathbf{U}_{g1} + \mathbf{U}_{g2} + \mathbf{U}_{g3} = 0$ is shown.

make an extra contribution to the statistical fluctuations in the estimated ABS.

3. VALIDATING THE ESTIMATOR

We validate the estimator by simulating a non-Gaussian sky signal $\delta T_b(\boldsymbol{\theta})$ for which the analytical expression for the ABS is known. We start from a Gaussian random field $\delta T_G(\boldsymbol{\theta})$ generated using an input model APS $C_\ell = (\ell/\ell_0)^{-1} \exp[-\ell^2/(\pi\ell_0)^2]$ mK² with $\ell_0 = 1000$. The non-Gaussian random field $\delta T_b(\boldsymbol{\theta})$ is obtained using a local non-linear transformation,

$$\delta T_b(\boldsymbol{\theta}) = \delta T_G(\boldsymbol{\theta}) + \frac{f_{\text{NG}}}{\sigma_T} (\delta T_G^2(\boldsymbol{\theta}) - \sigma_T^2), \quad (13)$$

where the dimensionless parameter f_{NG} controls the level of non-Gaussianity, and σ_T is the standard deviation of $\delta T_G(\boldsymbol{\theta})$. The analytical expression for the ABS of $\delta T_b(\boldsymbol{\theta})$ calculated to the first order in f_{NG} is (see appendix B for the details),

$$B_{\text{Ana}}(\ell_1, \ell_2, \ell_3) = \frac{2f_{\text{NG}}}{\sigma_T} (C_{\ell_1} C_{\ell_2} + C_{\ell_2} C_{\ell_3} + C_{\ell_3} C_{\ell_1}), \quad (14)$$

which is valid for $f_{\text{NG}} \ll 1$. Here we have used $f_{\text{NG}} = 0.17$, for which the ABS estimated from the simulated sky signal was found to be consistent with the predictions of Eq. (14).

The MWA baselines, for the data considered here, are mostly ($\sim 99\%$) within $U = 250$ (Chatterjee et al. 2023) that corresponds to $\ell = 1570$, which is an angular scale of 0.115° . Here, we have simulated the sky signal on a flat 2D grid of spacing 0.029° , which spans 117.35° that is ~ 4.5 times larger than θ_F . We have chosen this large range of angles to avoid abruptly cutting off the simulated signal at either the small angular scales or the large angular scales. The Gaussian factor in C_ℓ smoothly cuts off the signal at the smallest angular scales on the grid. We have multiplied the simulated $\delta T_b(\boldsymbol{\theta})$ with $A(\boldsymbol{\theta})$ (Eq. 5), and used a DFT (Eq. 4) to calculate the simulated $\mathcal{V}(\mathbf{U})$. The primary beam pattern $A(\boldsymbol{\theta})$ smoothly cuts off the sky signal from the largest angular scales ($\theta > \theta_F$) on the grid. In principle, we should use a spherical sky to perform these simulations (e.g., Chatterjee et al. 2023), however, the simulations are significantly faster if we use the flat sky approximation adopted here. Further, the subsequent analysis is restricted to the range $20 \leq \ell \leq 1570$ where we expect the flat sky approximation to hold (Datta et al. 2007).

We have gridded the visibilities (Eq. 9) using a grid spacing of $\Delta U_g = \sqrt{\ln 2}/\pi\theta_0 \approx 1$. Here, instead of correlating the visibilities $\mathcal{V}(\mathbf{U})$ at three baselines that form a closed triangle (Eq. 8), we estimate the ABS by correlating \mathcal{V}_g at three grid points that form a closed triangle. The different baselines that contribute to the three grid points generally do not form closed triangles. The relatively small grid spacing used here ensures that the factor $e^{-(\pi^2\theta_0^2\Delta U^2/3)}$ that arises in Eq. (8) due to this does not fall much below 1. We find that this factor has a value of 0.89 for a typical value of $(\Delta U)^2 = (\Delta U_g)^2/2$.

We have divided the (u, v) plane (Fig. 1) into 22 concentric annular rings of varying width, with a single ring of width 4 spanning radius 1 to 5 (in grid units), nine equally spaced rings between radii 5 and 50, five between 50 and 100, five between 100 and 200, and two between 200 and 250. We have used Eq. (12) to estimate $B(\ell_1, \mu, t)$ for every possible combination of three annular rings. Each estimated $\hat{B}(\ell_1, \mu, t)$ corresponds to the average ABS for all possible closed triangles that have one \mathbf{U} respectively in each of the three annular rings, as illustrated in Fig. 1. The bin widths have been progressively increased with U to account for the fact that the expected signal $B(\ell_1, \mu, t)$ and the baseline number density both go down with increasing U . Choosing a larger number of finer rings would provide estimates of the ABS at small intervals of (ℓ_1, μ, t) , at the cost of increasing the computation time, whereas choosing a smaller number of coarser rings would have the opposite effect. For the choice of rings adopted here, the different estimates of $\hat{B}(\ell_1, \mu, t)$ do not occur at equal intervals in the (ℓ_1, μ, t) parameter space. We have divided the ℓ_1 range into bins of equal logarithmic spacing, and the μ and t ranges into bins of equal linear spacing, and averaged

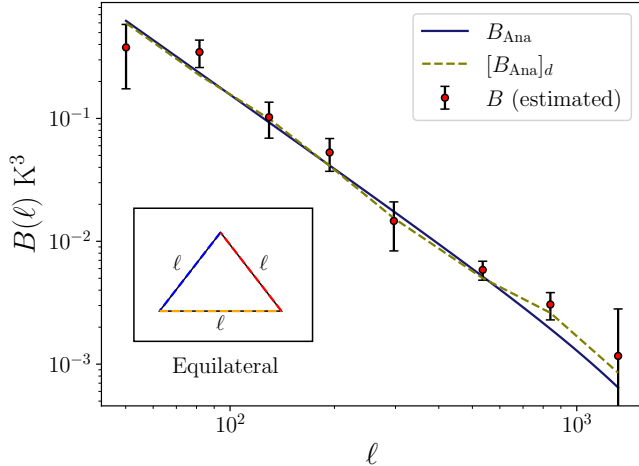


Figure 2. Validation of the estimator. Results are shown for the equilateral triangle at various angular multipoles ℓ . The red circles show the estimated bispectrum from simulated MWA visibility data, and the error bars show r.m.s. statistical fluctuations of the estimates computed using 500 independent realizations. The blue solid line shows the analytical predictions (Eq.14). The green dashed line shows the analytical prediction computed by incorporating the discrete sampling of the ℓ modes available in the data for each bin.

(weighted by the number of triangles) the $\hat{B}(\ell_1, \mu, t)$ values that occur in each bin.

We have used 500 statistically independent realizations of the random field to obtain reliable estimates of the ensemble average $B(\ell_1, \mu, t) = \langle \hat{B}(\ell_1, \mu, t) \rangle$ and the variance $\sigma^2 = \langle [\hat{B}(\ell_1, \mu, t)]^2 \rangle - [B(\ell_1, \mu, t)]^2$, for which the results are presented in the next section.

4. RESULTS

Fig. 2 shows the results considering equilateral triangles ($\mu \approx 0.5, t \approx 1$), for which the ABS is predicted to be $B_{\text{Ana}}(\ell) = 6 (f_{\text{NG}}/\sigma_T) C \ell^2$ (Eq. 14) which is represented by the blue solid line. The red circles show the binned ABS $B(\ell)$ estimated from the simulated visibilities, whereas the error bars show the 1σ r.m.s. statistical fluctuations. Each $B(\ell)$ shown here corresponds to the average of values estimated at some discrete ℓ , the exact set of ℓ values available within each bin depends on the choice of annular rings (Fig. 1). To account for this, we also show the analytic prediction $[B_{\text{Ana}}]_d$ (green dashed line) which incorporates the same discrete sampling as the actual data. We see that $B_{\text{Ana}}(\ell)$ and $[B_{\text{Ana}}]_d$ are nearly indistinguishable for $\ell < 600$ ($U < 100$), however, we have a noticeable (but relatively small) difference at larger ℓ where we have used wider annular rings. We find that the estimated $B(\ell)$ are consistent with $[B_{\text{Ana}}]_d$, and the deviations are within $\pm 1\sigma$ for $\ell \geq 80$. The deviations are within $\pm 2\sigma$ for $\ell < 80$, which may also be interpreted as arisen due to statistical fluctuations. The estimated $B(\ell)$ are all consistent with B_{Ana} also within 2σ . There is one more estimate at

$\ell \approx 20$, which deviates significantly due to the convolution with the primary beam, and we have not shown this here.

Fig. 3 provides a comprehensive validation of the estimator, considering triangles of all possible shapes (μ, t) and sizes ℓ_1 . Each panel of Fig. 3 is equivalent to Fig. 2, but for a different triangle shape. Each panel shows $B(\ell_1, \mu, t)$ as a function of ℓ_1 for a fixed set of (μ, t). We have divided the allowed range $0.5 \leq \mu, t \leq 1$ into 5×5 linear bins, and show results only for the bins that fall within the allowed region $2\mu t \geq 1$. The reader is referred to Fig. 2 of Bharadwaj et al. (2020) for a detailed discussion of the location of various triangle shapes in the $\mu - t$ plane. The upper left corner corresponds to equilateral triangles, for which the results have already been presented in Fig. 2. The upper and lower boundaries, respectively, correspond to isosceles triangles of two different types, whereas the right boundary corresponds to linear triangles, where the three sides are aligned in nearly the same direction. The upper and lower right corners respectively correspond to squeezed ($\ell_1 \approx \ell_2, \ell_3 \rightarrow 0$) and stretched ($\ell_1/2 \approx \ell_2 \approx \ell_3$) triangles.

We see that the results shown in the different panels of Fig. 3 are broadly very similar to those shown in Fig. 2, which has already been discussed in some details. However, there are also some differences that we highlight below. First, note that the available ℓ_1 range depends on the shape of the triangle, and we have the maximum ℓ_1 range for equilateral and squeezed triangles. The exact ℓ_1 range available for any shape is decided by the sizes of the annular rings that we have used. The relative sizes of the 1σ error bars also show considerable variation. These are typically large for low ℓ_1 , and decrease with larger ℓ_1 . The error bars also vary with the triangle shape, and these are smaller near the squeezed triangles. Both of these features are related to the number of available triangles. In general, we see that most values of $B(\ell_1, \mu, t)$ agree well with $[B_{\text{Ana}}]_d$, broadly validating our estimator. The subsequent results provides a more quantitative comparison between $B(\ell_1, \mu, t)$ and $[B_{\text{Ana}}]_d(\ell_1, \mu, t)$.

The left panel of Fig. 4 shows the (μ, t) dependence of $B(\ell_1, \mu, t)$, considering the fixed value $\ell_1 = 819$ for which all shapes are well sampled (Fig. 3). We see that the value of $B(\ell_1, \mu, t)$ is the maximum for squeezed triangles, which occurs in the upper right corner. The value of $B(\ell_1, \mu, t)$ decreases relatively faster along μ as compared to t , and $B(\ell_1, \mu, t)$ is minimum for equilateral triangles. We have $B(\ell_1, \mu, t) \propto \ell_1^{-2}$, and we may expect a similar (μ, t) dependence for other ℓ_1 also, barring effects due to the discrete sampling. The middle panel shows $[B_{\text{Ana}}]_d(\ell_1, \mu, t)$ for the same ℓ_1 value. We see that $B(\ell_1, \mu, t)$ and $[B_{\text{Ana}}]_d(\ell_1, \mu, t)$ both show very similar behavior. The right panel shows the fractional deviation $\Delta_B = |B - [B_{\text{Ana}}]_d|/[B_{\text{Ana}}]_d$. We see that most of the values of Δ_B are well within 15%, except for

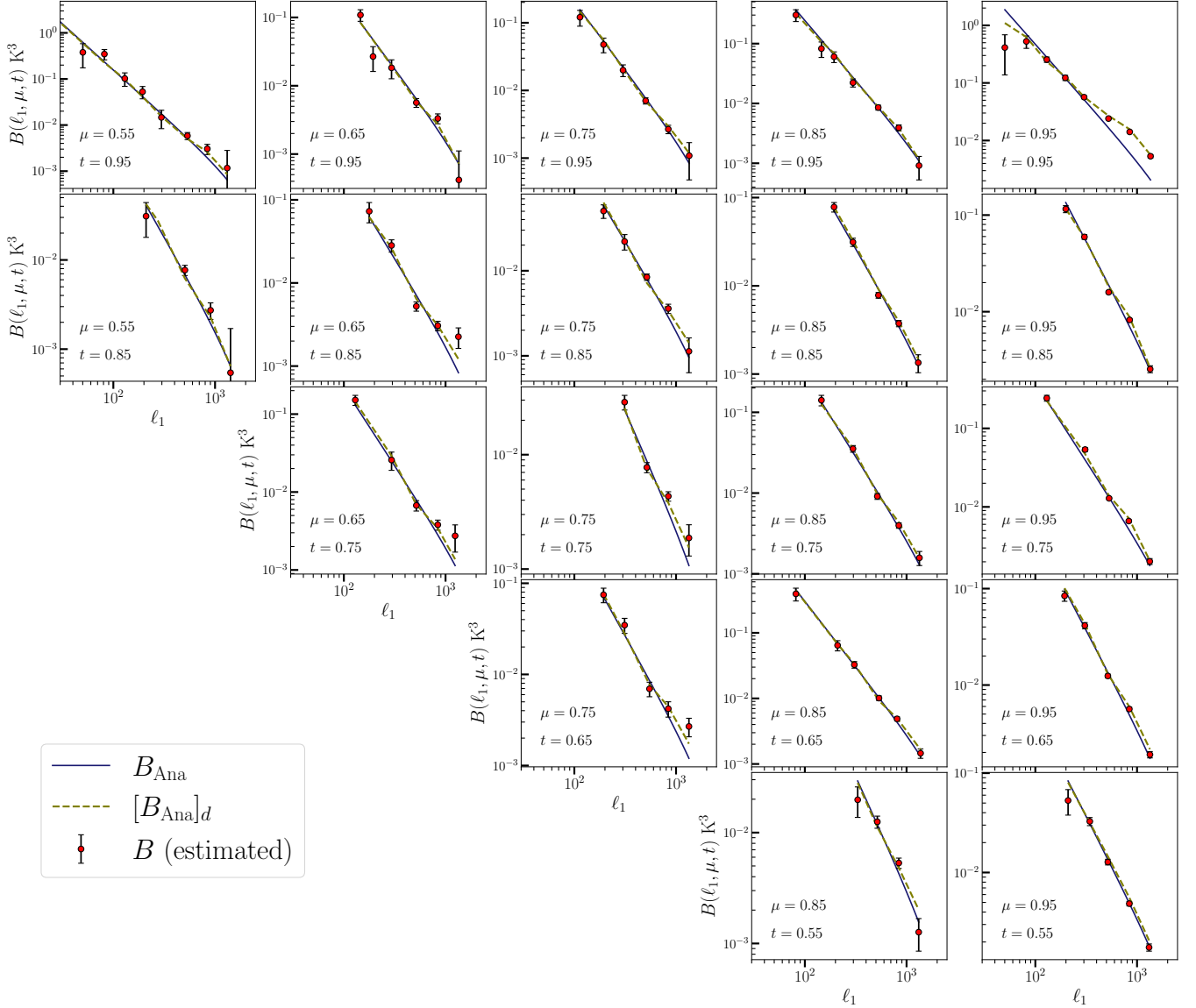


Figure 3. The upper left panel, which shows $B(\ell_1, \mu, t)$ as a function of ℓ_1 for $(\mu, t) = (0.55, 0.95)$ fixed, is exactly the same as Fig. 2 that considers equilateral triangles. The other panels are similar, but each corresponds to different values of (μ, t) , which corresponds to a different triangle shape. The panels span the entire allowed range of (μ, t) values, covering triangles of all possible shapes (refer to Fig. 2 of Bharadwaj et al. 2020).

three bins near the equilateral triangle where the fractional deviation has values $\approx 15 - 20\%$.

We have considered the ratio $\Delta_\sigma = |B - [B_{\text{Ana}}]_d|/\sigma$ to analyze whether the deviations between the estimated values $B(\ell_1, \mu, t)$ and the predicted values $[B_{\text{Ana}}]_d(\ell_1, \mu, t)$ are consistent with those expected from statistical fluctuations or not. The different panels of Fig 5 correspond to different values of ℓ_1 , starting from $\ell_1 = 46$ in the upper left corner and increasing clockwise to $\ell_1 = 1320$ in the bottom left corner. Each panel shows Δ_σ as a function of μ and t . We do not show results for the smallest bin $\ell_1 = 22$ where we have only a single estimate at the equilateral triangle, for which $\Delta_\sigma \leq 2$ is consistent with statistical fluctuations. Consid-

ering the smallest ℓ_1 , we have estimates for only two (μ, t) bins, namely the equilateral and squeezed triangles, for which we have $\Delta_\sigma \leq 2$ and ≤ 3 , respectively. The (μ, t) coverage increases for larger ℓ_1 , and we have full coverage for all the panels in the lower row. Taking all panels together, we have $\Delta_\sigma \leq 2$ for the majority of bins. There are a few bins where $2 < \Delta_\sigma \leq 3$, and only three bins where $3 < \Delta_\sigma \leq 5$. In general, we may interpret the deviations between $B(\ell_1, \mu, t)$ and $[B_{\text{Ana}}]_d(\ell_1, \mu, t)$ to be consistent with statistical fluctuations. The three bins where $3 < \Delta_\sigma \leq 5$ all occur near the squeezed limit ($\ell_1 \approx \ell_2, \ell_3 \rightarrow 0$) where, possibly, the deviations are not entirely due to statistical fluctuations. Here, a part of the deviation may arise because the bispectrum is very sensitive

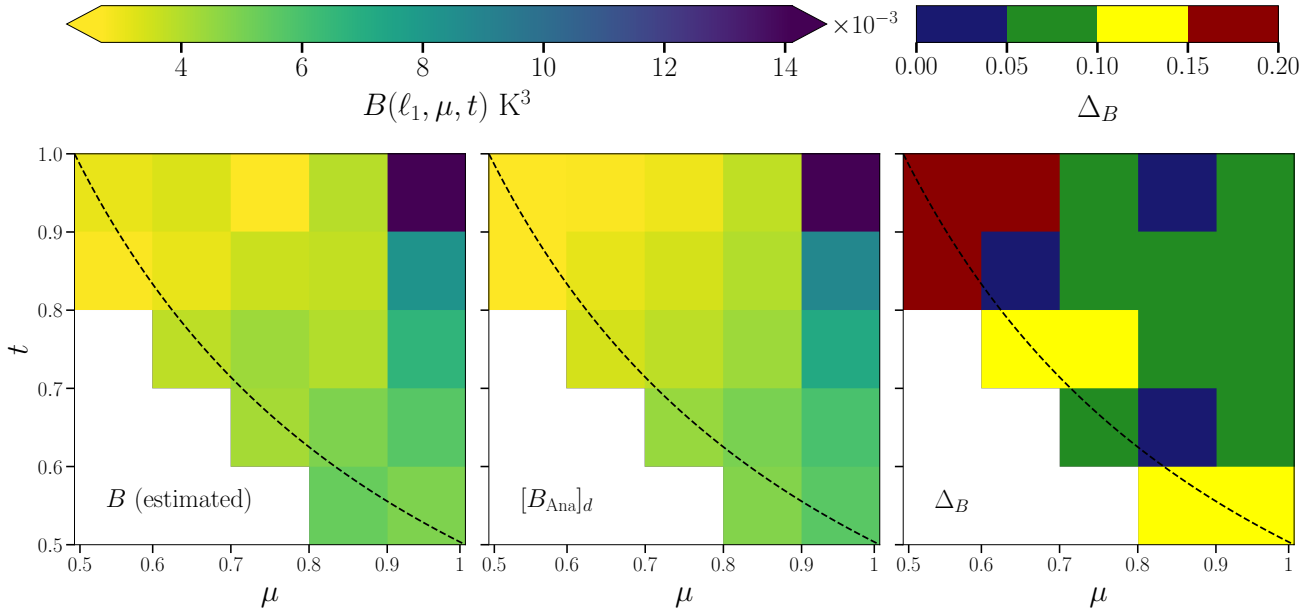


Figure 4. The left panel shows the estimated bispectrum $B(\ell_1, \mu, t)$ as a function of (μ, t) at $\ell_1 = 819$ fixed. Here μ and t parameterize the shape of a triangle. The allowed parameter range that is bounded within $2\mu t = 1$ (dashed line) and $0.5 \leq \mu, t \leq 1$ uniquely covers triangles of all possible shapes. The middle panel shows the analytic prediction $[B_{\text{Ana}}]_d$, and the right panel shows $\Delta_B = |B - [B_{\text{Ana}}]_d|/B$ the fractional deviations of the estimates from the predicted values.

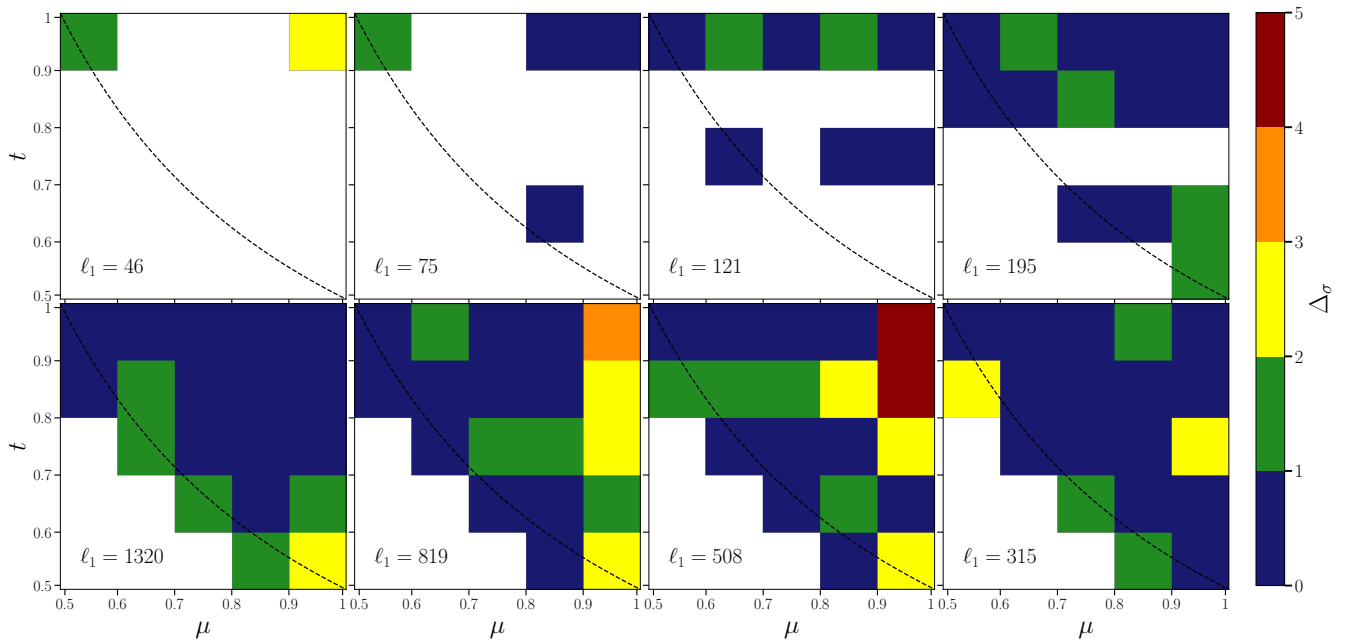


Figure 5. Each panel considers a different ℓ_1 , for which it shows $\Delta_\sigma = |B - [B_{\text{Ana}}]_d|/\sigma$ as a function of (μ, t) . Here Δ_σ is the difference between the estimated bispectrum (B) and the analytic prediction ($[B_{\text{Ana}}]_d$), expressed in units of the expected statistical fluctuations σ . The value of ℓ_1 increases clockwise starting from the upper left panel. Here μ and t parameterize the shape of a triangle. The allowed parameter range that is bounded within $2\mu t = 1$ (dashed line) and $0.5 \leq \mu, t \leq 1$ uniquely covers triangles of all possible shapes.

to the exact triangle configuration near the squeezed limit that considers $\ell_3 \rightarrow 0$, and the value of the bispectrum changes very rapidly even within the bin (Shaw et al. 2021; Gill & Bharadwaj 2024).

5. SUMMARY AND CONCLUSION

There is considerable motivation to quantify the three-point statistics of the radio sky. In this work, we have considered radio-interferometric observations, for which we present a visibility-based estimator for the angular bispectrum. The three-visibility correlation directly probes the bispectrum (Bharadwaj & Pandey 2005). However, the computational cost, which scales as the cube of the number of visibilities, makes it impractical to implement a direct correlation. Here we deal with the gridded visibilities instead. Although this reduces the computation, it still scales as the fourth power of the total number of grid points N_t , which can be computationally expensive. Here, we have implemented an FFT based fast estimator (Sefusatti 2005; Jeong 2010; Scoccimarro 2015) where the computation time scales as $\propto N_t^2 \log(N_t^2)$. Here, we follow Shaw et al. (2021) to present a binned angular bispectrum estimator $\hat{B}(\ell_1, \mu, t)$, where the angular multipole ℓ_1 and the dimensionless parameters (μ, t) respectively quantify the size and shape of the triangle. For the analysis presented in this work, it takes ~ 5 seconds to perform all the FFTs and ~ 1 minute 10 seconds to compute the ABS corresponding to all possible triangles for a single realization on a single core CPU.

We have used the simulated 154.25 MHz MWA observations (Patwa et al. 2021) to validate our estimator. We have

simulated visibility data considering a sky signal that has a known input model angular bispectrum. We find that these observations can be used to probe the angular bispectrum over a wide range of triangle sizes ($46 \leq \ell_1 \leq 1320$), and shapes. The estimated values are found to be in good agreement with the model predictions, and the deviations between these two are largely consistent with those expected from statistical fluctuations. Our analysis validates the estimator and demonstrates that the MWA observations considered here have the potential to quantify the angular bispectrum with $\approx 10 - 15\%$ accuracy. The analysis presented here does not take into account real observed data which includes foregrounds, system noise and possible systematics. In future work, we plan to apply our estimator to analyze the actual MWA data. We also plan to generalize the estimator so as to quantify the three-dimensional bispectrum of redshifted 21-cm brightness temperature fluctuations. A proper foreground removal or avoidance and mitigation of possible systematics are crucial to detect the 21-cm bispectrum using radio-interferometric observations.

ACKNOWLEDGEMENTS

The authors thank the anonymous reviewer for valuable suggestions and comments. SSG acknowledges the support of the Prime Minister Research Fellowship (PMRF).

DATA AVAILABILITY

The simulated data and package involved in this work will be shared on reasonable request to the authors.

REFERENCES

- Ali, S. S., Bharadwaj, S., & Chengalur, J. N. 2008, MNRAS, 385, 2166, doi: [10.1111/j.1365-2966.2008.12984.x](https://doi.org/10.1111/j.1365-2966.2008.12984.x)
- Ali, S. S., Bharadwaj, S., & Pandey, S. K. 2006, Mon. Not. Roy. Astron. Soc., 366, 213, doi: [10.1111/j.1365-2966.2005.09847.x](https://doi.org/10.1111/j.1365-2966.2005.09847.x)
- Bag, S., Mondal, R., Sarkar, P., et al. 2019, MNRAS, 485, 2235, doi: [10.1093/mnras/stz532](https://doi.org/10.1093/mnras/stz532)
- Bag, S., Mondal, R., Sarkar, P., Bharadwaj, S., & Sahni, V. 2018, MNRAS, 477, 1984, doi: [10.1093/mnras/sty714](https://doi.org/10.1093/mnras/sty714)
- Begum, A., Chengalur, J. N., & Bhardwaj, S. 2006, MNRAS, 372, L33, doi: [10.1111/j.1745-3933.2006.00220.x](https://doi.org/10.1111/j.1745-3933.2006.00220.x)
- Bernardi, G., de Bruyn, A. G., Brentjens, M. A., et al. 2009, A&A, 500, 965, doi: [10.1051/0004-6361/200911627](https://doi.org/10.1051/0004-6361/200911627)
- Bharadwaj, S., & Ali, S. S. 2005, MNRAS, 356, 1519, doi: [10.1111/j.1365-2966.2004.08604.x](https://doi.org/10.1111/j.1365-2966.2004.08604.x)
- Bharadwaj, S., Mazumdar, A., & Sarkar, D. 2020, MNRAS, 493, 594, doi: [10.1093/mnras/staa279](https://doi.org/10.1093/mnras/staa279)
- Bharadwaj, S., Pal, S., Choudhuri, S., & Dutta, P. 2018, Monthly Notices of the Royal Astronomical Society, 483, 5694, doi: [10.1093/mnras/sty3501](https://doi.org/10.1093/mnras/sty3501)
- Bharadwaj, S., & Pandey, S. K. 2005, MNRAS, 358, 968, doi: [10.1111/j.1365-2966.2005.08836.x](https://doi.org/10.1111/j.1365-2966.2005.08836.x)
- Bharadwaj, S., & Sethi, S. K. 2001, Journal of Astrophysics and Astronomy, 22, 293, doi: [10.1007/BF02702273](https://doi.org/10.1007/BF02702273)
- Chatterjee, S., Bharadwaj, S., Choudhuri, S., Sethi, S., & Patwa, A. K. 2023, MNRAS, 519, 2410, doi: [10.1093/mnras/stac3576](https://doi.org/10.1093/mnras/stac3576)
- Chatterjee, S., Elahi, K. M. A., Bharadwaj, S., et al. 2024, PASA, 41, e077, doi: [10.1017/pasa.2024.45](https://doi.org/10.1017/pasa.2024.45)
- Choudhuri, S., Bharadwaj, S., Ghosh, A., & Ali, S. S. 2014, Monthly Notices of the Royal Astronomical Society, 445, 4351, doi: [10.1093/mnras/stu2027](https://doi.org/10.1093/mnras/stu2027)
- Choudhuri, S., Bharadwaj, S., Ghosh, A., & Ali, S. S. 2014, MNRAS, 445, 4351, doi: [10.1093/mnras/stu2027](https://doi.org/10.1093/mnras/stu2027)
- Cooray, A., Li, C., & Melchiorri, A. 2008, PhRvD, 77, 103506, doi: [10.1103/PhysRevD.77.103506](https://doi.org/10.1103/PhysRevD.77.103506)

- Datta, K. K., Choudhury, T. R., & Bharadwaj, S. 2007, MNRAS, 378, 119, doi: [10.1111/j.1365-2966.2007.11747.x](https://doi.org/10.1111/j.1365-2966.2007.11747.x)
- DeBoer, D. R., Parsons, A. R., Aguirre, J. E., et al. 2017, PASP, 129, 045001, doi: [10.1088/1538-3873/129/974/045001](https://doi.org/10.1088/1538-3873/129/974/045001)
- Dutta, P., Begum, A., Bharadwaj, S., & Chengalur, J. N. 2009, MNRAS, 398, 887, doi: [10.1111/j.1365-2966.2009.15105.x](https://doi.org/10.1111/j.1365-2966.2009.15105.x)
- Ghosh, A., Prasad, J., Bharadwaj, S., Ali, S. S., & Chengalur, J. N. 2012, MNRAS, 426, 3295, doi: [10.1111/j.1365-2966.2012.21889.x](https://doi.org/10.1111/j.1365-2966.2012.21889.x)
- Gill, S. S., & Bharadwaj, S. 2024, arXiv e-prints, arXiv:2405.14513, doi: [10.48550/arXiv.2405.14513](https://doi.org/10.48550/arXiv.2405.14513)
- Gill, S. S., Pramanick, S., Bharadwaj, S., Shaw, A. K., & Majumdar, S. 2024, MNRAS, 527, 1135, doi: [10.1093/mnras/stad3273](https://doi.org/10.1093/mnras/stad3273)
- Jeong, D. 2010, PhD thesis, Cosmology with high ($z > 1$) redshift galaxy surveys, Univ. Texas at Austin
- Kamran, M., Ghara, R., Majumdar, S., et al. 2021, MNRAS, 502, 3800, doi: [10.1093/mnras/stab216](https://doi.org/10.1093/mnras/stab216)
- Line, J. L. B., McKinley, B., Rasti, J., et al. 2018, PASA, 35, e045, doi: [10.1017/pasa.2018.30](https://doi.org/10.1017/pasa.2018.30)
- Majumdar, S., Kamran, M., Pritchard, J. R., et al. 2020, Mon. Not. Roy. Astron. Soc., 499, 5090, doi: [10.1093/mnras/staa3168](https://doi.org/10.1093/mnras/staa3168)
- Majumdar, S., Pritchard, J. R., Mondal, R., et al. 2018, Mon. Not. Roy. Astron. Soc., 476, 4007, doi: [10.1093/mnras/sty535](https://doi.org/10.1093/mnras/sty535)
- Nunhokee, C. D., Parsons, A. R., Kern, N. S., et al. 2020, ApJ, 897, 5, doi: [10.3847/1538-4357/ab9634](https://doi.org/10.3847/1538-4357/ab9634)
- Patwa, A. K., Sethi, S., & Dwarakanath, K. S. 2021, MNRAS, 504, 2062, doi: [10.1093/mnras/stab989](https://doi.org/10.1093/mnras/stab989)
- Pillepich, A., Porciani, C., & Matarrese, S. 2007, ApJ, 662, 1, doi: [10.1086/517963](https://doi.org/10.1086/517963)
- Raste, J., Kulkarni, G., Watkinson, C. A., Keating, L. C., & Haehnelt, M. G. 2023, arXiv e-prints, arXiv:2308.09744, <https://arxiv.org/abs/2308.09744>
- Roy, N., Bharadwaj, S., Dutta, P., & Chengalur, J. N. 2009, Mon. Not. Roy. Astron. Soc., 393, 26, doi: [10.1111/j.1745-3933.2008.00591.x](https://doi.org/10.1111/j.1745-3933.2008.00591.x)
- Saha, P., Bharadwaj, S., Chakravorty, S., et al. 2021, MNRAS, 502, 5313, doi: [10.1093/mnras/stab446](https://doi.org/10.1093/mnras/stab446)
- Saha, P., Bharadwaj, S., Roy, N., Choudhuri, S., & Chattopadhyay, D. 2019, Monthly Notices of the Royal Astronomical Society, 489, 5866, doi: [10.1093/mnras/stz2528](https://doi.org/10.1093/mnras/stz2528)
- Sarkar, D., Majumdar, S., & Bharadwaj, S. 2019, Mon. Not. Roy. Astron. Soc., 490, 2880, doi: [10.1093/mnras/stz2799](https://doi.org/10.1093/mnras/stz2799)
- Scoccimarro, R. 2015, PhRvD, 92, 083532, doi: [10.1103/PhysRevD.92.083532](https://doi.org/10.1103/PhysRevD.92.083532)
- Sefusatti, E. 2005, PhD thesis, Probing fundamental physics with large-scale structure: From galaxy formation to inflation, Polytechnic University, United States
- Sefusatti, E., Crocce, M., Pueblas, S., & Scoccimarro, R. 2006, PhRvD, 74, 023522, doi: [10.1103/PhysRevD.74.023522](https://doi.org/10.1103/PhysRevD.74.023522)
- Shaw, A. K., Bharadwaj, S., Sarkar, D., et al. 2021, arXiv e-prints, arXiv:2107.14564, <https://arxiv.org/abs/2107.14564>
- Shimabukuro, H., Yoshiura, S., Takahashi, K., Yokoyama, S., & Ichiki, K. 2017, Mon. Not. Roy. Astron. Soc., 468, 1542, doi: [10.1093/mnras/stx530](https://doi.org/10.1093/mnras/stx530)
- The HERA Collaboration., 2022, The Astrophysical Journal, 925, 221, doi: [10.3847/1538-4357/ac1c78](https://doi.org/10.3847/1538-4357/ac1c78)
- Tingay, S. J., Goeke, R., Bowman, J. D., et al. 2013, PASA, 30, e007, doi: [10.1017/pasa.2012.007](https://doi.org/10.1017/pasa.2012.007)
- Trott, C. M., et al. 2019, Publ. Astron. Soc. Austral., 36, e023, doi: [10.1017/pasa.2019.15](https://doi.org/10.1017/pasa.2019.15)
- van Haarlem, M. P., Wise, M. W., Gunst, A. W., et al. 2013, A&A, 556, A2, doi: [10.1051/0004-6361/201220873](https://doi.org/10.1051/0004-6361/201220873)
- Virone, G., Paonessa, F., Ciorba, L., et al. 2022, Journal of Astronomical Telescopes, Instruments, and Systems, 8, 011005, doi: [10.1117/1.JATIS.8.1.011005](https://doi.org/10.1117/1.JATIS.8.1.011005)
- Watkinson, C. A., Giri, S. K., Ross, H. E., et al. 2019, Mon. Not. Roy. Astron. Soc., 482, 2653, doi: [10.1093/mnras/sty2740](https://doi.org/10.1093/mnras/sty2740)
- Watkinson, C. A., Greig, B., & Mesinger, A. 2022, MNRAS, 510, 3838, doi: [10.1093/mnras/stab3706](https://doi.org/10.1093/mnras/stab3706)
- Wayth, R. B., Tingay, S. J., Trott, C. M., et al. 2018, PASA, 35, e033, doi: [10.1017/pasa.2018.37](https://doi.org/10.1017/pasa.2018.37)

APPENDIX

A. TWO AND THREE VISIBILITY CORRELATIONS

We present a brief derivation of Eq. 7 and Eq. 8. It is convenient to work in the continuum limit where Eq. 1, 2 and 3 are respectively given by

$$\delta T_b(\boldsymbol{\theta}) = \int \frac{d^2\ell}{(2\pi)^2} \exp[-i\boldsymbol{\ell} \cdot \boldsymbol{\theta}] \Delta \tilde{T}_b(\boldsymbol{\ell}) , \quad (\text{A1})$$

$$\langle \Delta \tilde{T}_b(\boldsymbol{\ell}) \Delta \tilde{T}_b^*(\boldsymbol{\ell}') \rangle = (2\pi)^2 \delta_D^2(\boldsymbol{\ell} - \boldsymbol{\ell}') C_\ell \quad (\text{A2})$$

and

$$\langle \Delta \tilde{T}_b(\boldsymbol{\ell}_1) \Delta \tilde{T}_b(\boldsymbol{\ell}_2) \Delta \tilde{T}_b(\boldsymbol{\ell}_3) \rangle = (2\pi)^2 \delta_D^2(\boldsymbol{\ell}_1 + \boldsymbol{\ell}_2 + \boldsymbol{\ell}_3) B(\ell_1, \ell_2, \ell_3) \quad (\text{A3})$$

where $\delta_D^2(\boldsymbol{\ell} - \boldsymbol{\ell}')$ is the 2D Dirac delta function. We also define the aperture power pattern

$$\tilde{a}(\mathbf{U}) = \int d^2\theta A(\boldsymbol{\theta}) \exp[i2\pi\mathbf{U} \cdot \boldsymbol{\theta}] \quad (\text{A4})$$

which is the Fourier transform of $A(\boldsymbol{\theta})$. Using the convolution theorem, the visibility $\mathcal{V}(\mathbf{U})$ (Eq. 4) can be expressed as

$$\mathcal{V}(\mathbf{U}) = Q \int \frac{d^2\ell}{(2\pi)^2} \tilde{a}(\mathbf{U} - \boldsymbol{\ell}/(2\pi)) \Delta \tilde{T}_b(\boldsymbol{\ell}) , \quad (\text{A5})$$

For the Gaussian beam $A_G(\boldsymbol{\theta})$ given in Eq. 6, we have the Gaussian aperture power pattern

$$\tilde{a}_G(\mathbf{U}) = \pi\theta_0^2 \exp[-\pi^2\theta_0^2 U^2] . \quad (\text{A6})$$

The correlation of two visibilities corresponding to baselines \mathbf{U} and $\mathbf{U} + \Delta\mathbf{U}$ is given by,

$$\langle \mathcal{V}(\mathbf{U}) \mathcal{V}^*(\mathbf{U} + \Delta\mathbf{U}) \rangle = Q^2 \int \frac{d^2\ell'}{(2\pi)^2} \tilde{a}_G(\mathbf{U} - \boldsymbol{\ell}'/(2\pi)) \tilde{a}_G^*(\mathbf{U} + \Delta\mathbf{U} - \boldsymbol{\ell}'/(2\pi)) C_{\ell'} \quad (\text{A7})$$

We assume that the $C_{\ell'}$ does not change significantly within θ_0^{-1} the width of $\tilde{a}_G(\mathbf{U} - \boldsymbol{\ell}'/(2\pi))$ whereby we can hold its value constant at $\boldsymbol{\ell}' = 2\pi\mathbf{U}$ and take it outside the integral. We then have

$$\langle \mathcal{V}(\mathbf{U}) \mathcal{V}^*(\mathbf{U} + \Delta\mathbf{U}) \rangle = Q^2 \left[\int \frac{d^2\ell'}{(2\pi)^2} \tilde{a}_G(\mathbf{U} - \boldsymbol{\ell}'/(2\pi)) \tilde{a}_G^*(\mathbf{U} + \Delta\mathbf{U} - \boldsymbol{\ell}'/(2\pi)) \right] C_{\ell=2\pi U} \quad (\text{A8})$$

The expression in the square brackets is a standard two-dimensional Gaussian integral, yielding

$$\langle \mathcal{V}(\mathbf{U}) \mathcal{V}^*(\mathbf{U} + \Delta\mathbf{U}) \rangle = \frac{\pi\theta_0^2 Q^2}{2} \exp[-\pi^2\theta_0^2 \Delta U^2/2] C_\ell . \quad (\text{A9})$$

where $\ell = 2\pi U$.

We next consider the three-visibility correlation. Using Eq. A3, the correlation of three visibilities corresponding to baselines \mathbf{U}_1 , \mathbf{U}_2 and $\mathbf{U}_3 + \Delta\mathbf{U}$ is given by

$$\begin{aligned} \langle \mathcal{V}(\mathbf{U}_1) \mathcal{V}(\mathbf{U}_2) \mathcal{V}(\mathbf{U}_3 + \Delta\mathbf{U}) \rangle &= Q^3 \int \frac{d^2\ell'_1}{(2\pi)^2} \int \frac{d^2\ell'_2}{(2\pi)^2} \tilde{a}_G(\mathbf{U}_1 - \boldsymbol{\ell}'_1/(2\pi)) \tilde{a}_G(\mathbf{U}_2 - \boldsymbol{\ell}'_2/(2\pi)) \tilde{a}_G^*(\mathbf{U}_3 + \Delta\mathbf{U} - \boldsymbol{\ell}'_3/(2\pi)) \\ &\times B(\ell'_1, \ell'_2, \ell'_3) \end{aligned} \quad (\text{A10})$$

where $\boldsymbol{\ell}'_3 = -\boldsymbol{\ell}'_1 - \boldsymbol{\ell}'_2$.

Here we assume $\mathbf{U}_1 + \mathbf{U}_2 + \mathbf{U}_3 = 0$, that is, they form a closed triangle, and $\Delta\mathbf{U}$ quantifies the deviation from the closed triangle configuration. As in Eq. A8, here too we assume that $B(\ell'_1, \ell'_2, \ell'_3)$ does not vary significantly over the width of $\tilde{a}_G(\mathbf{U} - \boldsymbol{\ell}'_1/(2\pi))$

and $\tilde{a}_G(\mathbf{U} - \ell'_2/(2\pi))$. This allows us to replace $B(\ell'_1, \ell'_2, \ell'_3)$ with $B(\ell_1, \ell_2, \ell_3)$ where $\ell_1 = 2\pi\mathbf{U}_1$, $\ell_2 = 2\pi\mathbf{U}_2$ and $\ell_3 = 2\pi\mathbf{U}_3$, and write it outside the integral in Eq. A10. We then have

$$\langle \mathcal{V}(\mathbf{U}_1)\mathcal{V}(\mathbf{U}_2)\mathcal{V}(\mathbf{U}_3 + \Delta\mathbf{U}) \rangle = Q^3 \left[\int \frac{d^2\ell'_1}{(2\pi)^2} \int \frac{d^2\ell'_2}{(2\pi)^2} \tilde{a}_G(\mathbf{U}_1 - \ell'_1/(2\pi)) \tilde{a}_G(\mathbf{U}_2 - \ell'_2/(2\pi)) \tilde{a}_G^*(\mathbf{U}_3 + \Delta\mathbf{U} - \ell'_3/(2\pi)) \right] \times B(\ell_1, \ell_2, \ell_3) \quad (\text{A11})$$

The terms in the square bracket are a four-dimensional Gaussian integral. We evaluate this to obtain

$$\langle \mathcal{V}(\mathbf{U}_1)\mathcal{V}(\mathbf{U}_2)\mathcal{V}(\mathbf{U}_3 + \Delta\mathbf{U}) \rangle = \frac{\pi\theta_0^2 Q^3}{3} \exp[-\pi^2\theta_0^2\Delta U^2/3] B(\ell_1, \ell_2, \ell_3). \quad (\text{A12})$$

which is the relation between the three-visibility correlation and the ABS.

B. ANGULAR BISPECTRUM FOR OUR NON-GAUSSIAN MODEL

We provide a brief derivation of Eq. 14. The non-Gaussian model of brightness temperature fluctuations (Eq. 13) is given by the convolution in the Fourier space as,

$$\Delta\tilde{T}_b(\ell) = \Delta\tilde{T}_G(\ell) + \frac{f_{\text{NG}}}{\sigma_T} \frac{1}{(2\pi)^2} \int d^2\ell_1 \Delta\tilde{T}_G(\ell - \ell_1) \Delta\tilde{T}_G(\ell_1) \quad (\text{B13})$$

We proceed by substituting $\Delta\tilde{T}_b(\ell)$ (Eq. B13) into the definition of the ABS (Eq. A3). Note that the expectation value of the product of an odd number of Gaussian random fields is zero. The leading order nonzero term, in powers of $f_{\text{NG}} (\ll 1)$, is

$$(2\pi)^2 \delta_D^2(\ell_1 + \ell_2 + \ell_3) B_{\text{Ana}}(\ell_1, \ell_2, \ell_3) = \frac{f_{\text{NG}}}{\sigma_T} \left[\langle \Delta\tilde{T}_G(\ell_1)\Delta\tilde{T}_G(\ell_2) \int \frac{d^2\ell'}{(2\pi)^2} \Delta\tilde{T}_G(\ell_3 - \ell')\Delta\tilde{T}_G(\ell') \rangle + 2 \text{ terms} \right]. \quad (\text{B14})$$

The two other terms indicated above can be respectively obtained by interchanging ℓ_1 with ℓ_3 , and ℓ_2 with ℓ_3 . There are higher order terms in f_{NG} that we ignore.

Wick's theorem states that,

$$\langle \Delta\tilde{T}_G(\ell_1)\Delta\tilde{T}_G(\ell_2)\Delta\tilde{T}_G(\ell_3)\Delta\tilde{T}_G(\ell_4) \rangle = \langle \Delta\tilde{T}_G(\ell_1)\Delta\tilde{T}_G(\ell_2) \rangle \langle \Delta\tilde{T}_G(\ell_3)\Delta\tilde{T}_G(\ell_4) \rangle + \langle \Delta\tilde{T}_G(\ell_1)\Delta\tilde{T}_G(\ell_3) \rangle \langle \Delta\tilde{T}_G(\ell_2)\Delta\tilde{T}_G(\ell_4) \rangle + \langle \Delta\tilde{T}_G(\ell_1)\Delta\tilde{T}_G(\ell_4) \rangle \langle \Delta\tilde{T}_G(\ell_2)\Delta\tilde{T}_G(\ell_3) \rangle \quad (\text{B15})$$

Using Eqs. B15 and A2 in B14, we have,

$$(2\pi)^2 \delta_D^2(\ell_1 + \ell_2 + \ell_3) B_{\text{Ana}}(\ell_1, \ell_2, \ell_3) = \frac{f_{\text{NG}}}{\sigma_T} \left[\int d^2\ell' (2\pi)^2 \{ \delta_D^2(\ell_1 + \ell_2) \delta_D^2(\ell_3) C_{\ell_1} C_{\ell'} + \delta_D^2(\ell_1 + \ell_3 - \ell') \delta_D^2(\ell_2 + \ell') C_{\ell_1} C_{\ell_2} + \delta_D^2(\ell_1 + \ell') \delta_D^2(\ell_2 + \ell_3 - \ell') C_{\ell_1} C_{\ell_2} \} + 2 \text{ terms} \right]. \quad (\text{B16})$$

The first term on the RHS only contributes when $\ell_3 = 0$. This refers to the θ independent constant component of $\delta T_b(\theta)$, which is zero and can be ignored. Performing the ℓ' integral and including the other two terms, we obtain the final expression for the ABS to the first order in f_{NG} ,

$$B_{\text{Ana}}(\ell_1, \ell_2, \ell_3) = \frac{2f_{\text{NG}}}{\sigma_T} (C_{\ell_1} C_{\ell_2} + C_{\ell_2} C_{\ell_3} + C_{\ell_3} C_{\ell_1}), \quad (\text{B17})$$

where the three ℓ modes form a closed triangle, i.e., $\ell_1 + \ell_2 + \ell_3 = 0$.